Pergamon

The role of microcracking in shear-fracture propagation in granite

D. E. MOORE and D. A. LOCKNER

U.S. Geological Survey, MS/977 Menlo Park, CA 94025, U.S.A.

Abstract—Microcracking related to the formation of a laboratory shear fracture in a cylinder of Westerly granite has been investigated using image-analysis computer techniques. Well away from the fracture (farfield), the deformed granite has about twice the crack density (crack length per unit area) of undeformed granite. The microcrack density increases dramatically in a process zone that surrounds the fracture tip, and the fracture tip itself has more than an order of magnitude increase in crack density over the undeformed rock. Microcrack densities are consistently higher on the dilational side of the shear than on the compressional side. Microcracks in the undeformed rock and in the far-field areas of the laboratory sample are concentrated within and along the margins of quartz crystals, but near the shear fracture they are somewhat more abundant within K-feldspar crystals. The energy release rate, G_{II}, for mode II fracture propagation is estimated from the microcrack density data to be $\geq 1.7-8.6$ kJ m^{-2}. The microcracks that formed during the experiment are principally tensile cracks whose orientations reflect the local stress field: those formed prior to the nucleation of the fault are roughly parallel to the cylinder axis (loading direction), whereas those generated in the process zone make angles averaging 30° to the overall fault strike (and 20° to the cylinder axis). The preferred orientation and uneven distribution of microcracks in the process zone tends to pull the propagating fracture tip towards the dilational side, even though the trend is away from the overall fault strike. As a result, the propagating shear follows the microcrack trend for some distance and then changes direction in order to maintain an overall in-plane propagation path. This recurring process produces a zig-zag or sawtooth segmentation pattern similar to the sawtooth geometries of faults such as the San Andreas fault.

INTRODUCTION

There has been a long-standing need in rock mechanics for quantitative information on microcracking in both stressed and unstressed rocks. So far, very few investigations of this type have been undertaken, because the work is both time-consuming and tedious. Of those few, the majority are based on stereological estimates of crack densities (e.g. Tapponnier & Brace 1976, Fredrich & Wong 1986) rather than direct measurements of microcrack parameters (e.g. Hadley 1976), although the results obtained by the two methods seem to be comparable (Wong 1985). In recent years, image-analysis computer programs have been developed that facilitate both the direct measurement of crack lengths and orientations and the manipulation of the large amounts of data collected. This paper describes an investigation of the role of microcracking in shear-fracture propagation, using image-analysis techniques.

The sample we studied is a 19.5 cm-long cylinder of Westerly granite that was used in an experiment run dry at 50 MPa confining pressure to record acoustic emission (sample G2 of Lockner *et al.* 1992a). The experimental procedures permitted 'quasi-static' propagation of the shear fracture at rates less than 10 mm s^{-1}, rather than dynamic propagation at nearly shear-wave velocity as is more typical of catastrophic failure in laboratory samples. The shear fracture that formed during the experiment ceased to propagate before it reached the end of the cylinder, providing a rare opportunity to

examine the rock directly in front of the fracture tip. The record of acoustic emission events (Lockner *et al.* 1992a, fig. 8) suggests that microcrack formation during the experiment can be separated into two stages. Prior to sample failure microcracks were generated throughout the cylinder, whereas after the shear fracture formed, the microcracking was localized in a process zone surrounding the fracture tip. This process zone presumably migrated across the cylinder in advance of the propagating shear.

The major goals of this study are: (1) to provide estimates of microcrack densities associated with the shear fracture and preliminary energy calculations based on the density data; (2) to characterize and compare the two stages of microcracking in the sample; (3) to determine the controls, if any, of mineralogy on crack density; and (4) to investigate the relationships between the microcrack populations and the geometry of the shear fracture.

PROCEDURES

This work is a reconnaissance study to obtain a general idea of microcrack distributions in the sample. We wanted to examine a relatively large number of spots; in addition, we wanted each spot to comprise a sufficiently large area to be representative of the rock and to allow meaningful comparisons of the major minerals: quartz, plagioclase and K-feldspar. To make such an extensive
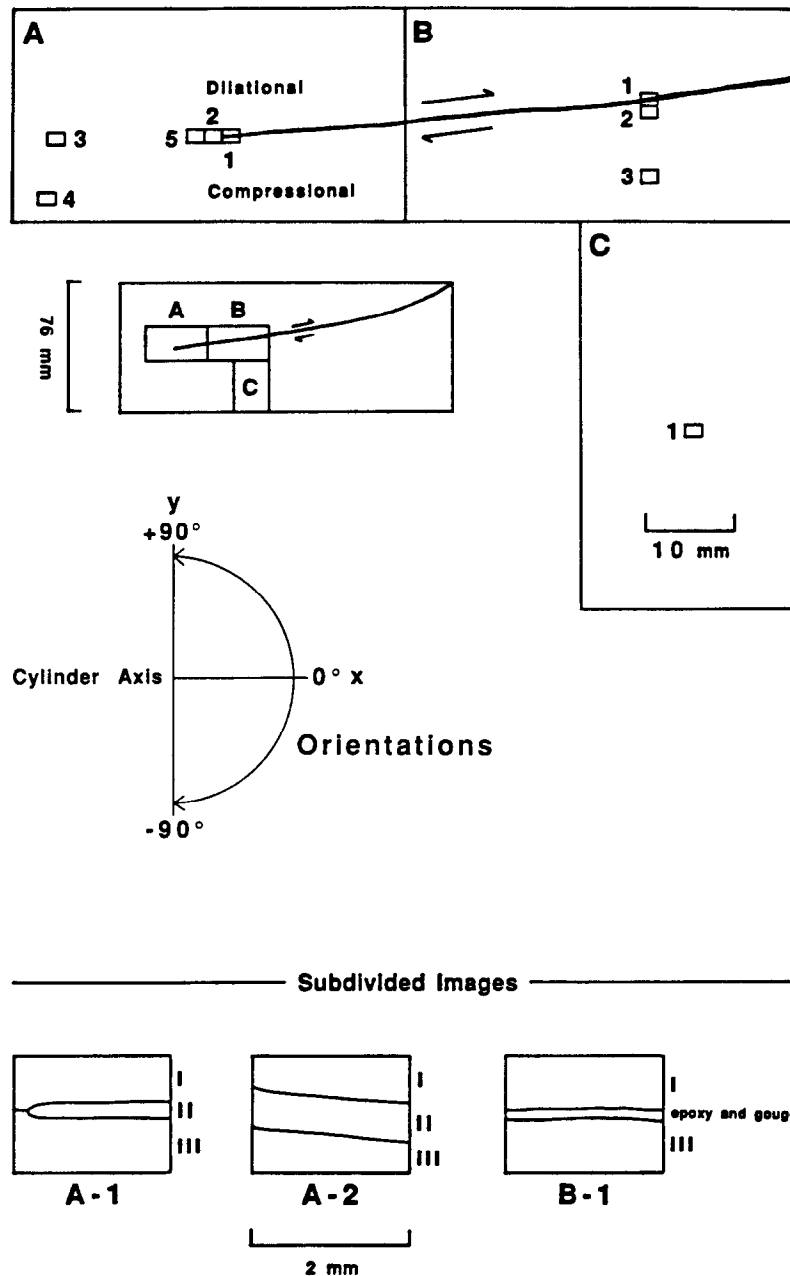
Fig. 1. Locations of the nine images examined from the stressed sample, and convention for reporting orientations and position. Images are labelled according to the letter designation of the thin section, followed by the image number in the section, e.g. A-3, B-1. An additional image of undeformed Westerly granite (not pictured), labelled WPS, was also examined. The three most densely cracked images were subdivided as shown, for comparison of total crack densities and orientations. Areas (mm^2) of subdivided images: A-1 (I = 1.21, II = 0.25, III = 1.54); A-2 (I = 1.17, II = 0.81, III = 1.02); B-1 (I = 1.24, III = 1.38).

study practicable, we limited our view to the magnification available in a petrographic microscope. In spite of its reconnaissance nature, the results of this study are consistent with other observations on microcracking in Westerly granite. It also appears that the largest cracks are the first to interact mechanically and therefore dominate both the fracture process and the transport properties of the rock (Madden 1983, Lockner & Madden 1991, Lockner et al. 1992b). As a result, many important processes related to microcrack growth can be examined by studying the larger cracks. The general experimental procedures are described below and in

Moore (1993). The complete data set for this study is also presented in Moore (1993).

After deformation, the granite cylinder was cut in half parallel to the cylinder axis and perpendicular to the shear fracture. Three polished thin sections of standard thickness (about 30 μm) were made from one of the half cylinders, as shown in Fig. 1. Sections A and B contain the final 70 mm of the shear fracture; the midpoint of the shear is about 90 mm from the tip. The fault makes a small angle of about 10° to the cylinder axis (Fig. 1). The size of this angle has been demonstrated to decrease with decreasing effective pressure (e.g. Paterson 1958, Tullis

& Yund 1977, Moore *et al.* 1990); the small angle, therefore, is consistent with the relatively low effective pressure of the experiment. Nine reflected-light images, each covering an area 2 mm × 1.5 mm in size, were scanned directly into a computer from a microscope; the locations of the images in the three thin sections are shown in Fig. 1. An additional image was collected from a small cylinder of the starting Westerly granite cored in the same direction into the granite block as the large cylinder. The circular cross-section of the large cylinder had not been oriented relative to the sides of the granite block prior to coring. As a result, thin sections from the large and small cylinders could show different vertical slices through the granite block. As discussed later, however, the thin sections probably differ in orientation by no more than a few degrees.

Images A-1 and B-1 were subdivided into regions above (I) and below (III) the shear fracture (Fig. 1) for comparison of their total crack densities. Image A-1 also contains a 0.1 mm-wide band of high crack density surrounding the fracture tip that was considered separately (zone II). Image A-2 was similarly divided into three parts: a central zone of high crack density (II) and less highly cracked areas above (I) and below (III). Had the fracture tip advanced further, it would undoubtedly have propagated across zone II of image A-2. The reported results for the areas of highest crack density in these three images are probably minimum values, because of the difficulties encountered in separating closely spaced cracks. In addition, gouge-forming processes have been initiated along the fracture at A-1 and are well advanced at B-1. No attempt was made to deal with the crushed granite, and the crack densities reported for A-1 and B-1 represent the more or less intact rock adjacent to the shear. Because of the variable sizes of some of the images and subdivided images (Fig. 1), all results are normalized to a 1 mm² area of granite, to facilitate comparisons. The various minerals in Westerly granite differ in their abundance; thus, reported intragranular crack densities for a given mineral are normalized to a 1 mm² area of that mineral to allow direct comparison of their densities.

Microcracks were identified under the microscope, and their lengths and orientations were measured on the calibrated computer image. The convention for reporting orientations is shown in Fig. 1. In cases where a long crack consists of a series of smaller, linked cracks, the individual small cracks were measured and counted separately. Most bent cracks are clearly seen to be two separate cracks that intersect at the bend, but a few bent or highly curved cracks have no obvious subdivisions. Similarly, some grain-boundary cracks appear to be continuously open around the corners of a crystal. Hadley (1976) subdivided cracks that changed orientation by more than 20°, and the same practice was adopted here for the apparently continuous but curved or bent cracks. The orientation of a given crack is the average over its length. The area of each crystal was also measured on the computer images, to determine mineral proportions.

Normal operating magnification under the microscope was 312×, with spot checks of individual cracks made at 500×. The shortest resolvable cracks were about 3 μm long; this was also the minimum length that could be measured for the image size scanned into the computer (the calibrated length of 1 screen pixel was 3.13 μm). Thus, the data have a lower crack-length cutoff of 3 μm. However, the results of Hadley (1976; see also table 1 of Madden 1983 and discussion by Wong 1985) indicate that the average crack length in Westerly increases in stressed samples, and that only the unstressed samples contain numerous cracks less than 3 μm long. Sprunt & Brace (1974) reached similar conclusions about crack lengths in stressed and unstressed samples. This suggests that the measurement limits will principally affect the results for the undeformed sample, and even there the omission of the shortest cracks will not significantly change the total crack length (Wong 1985).

RESULTS

Textural observations

This section focuses on those textural features that are relevant to the interpretation of the data. The reader is referred to Tapponnier & Brace (1976) for additional information on microcrack morphology in Westerly granite and to Kranz (1983 and references therein) for general information on microcracks. Westerly granite is one of the most commonly employed rock types in laboratory studies, because of its relatively fine grain size and apparent lack of a fabric. The grain size of Westerly granite ranges from about 0.05–2.2 mm (Moore *et al.* 1987); Chayes (1950a) reported a maximum crystal length of 2.5 mm. This modest size range is nevertheless significant at the scale of the examined images. Some of the images are dominated by large quartz and/or plagioclase crystals (Fig. 2a), whereas others are relatively fine-grained overall (Fig. 2c). Because of these size differences, the summed grain-boundary length in the different images varies substantially between 6 and 9 mm mm^{-2}.

The majority of the grain-boundary length in both the starting material and the laboratory sample is oriented in the range 0–90° (see Fig. 1 for orientation convention). The edges of relatively equant crystals tend to have orientations near 0° and 90°. Long, tabular crystals of plagioclase and platy crystals of biotite have a modest grain-shape alignment at about 50–60°, as illustrated by both the undeformed sample WPS and image A-1 in Fig. 2.

Some of the large plagioclase crystals in Westerly granite are mantled by K-feldspar; good examples can be seen on the upper left side of Fig. 2(a) and the upper right side of Fig. 2(c). Similarly mantled feldspars in the Barre granite of Vermont were considered by Chayes (1950b) to be a late-stage, igneous crystallization process, with the K-feldspar finding a preferred nucleation

(a)

WPS   0.25 mm

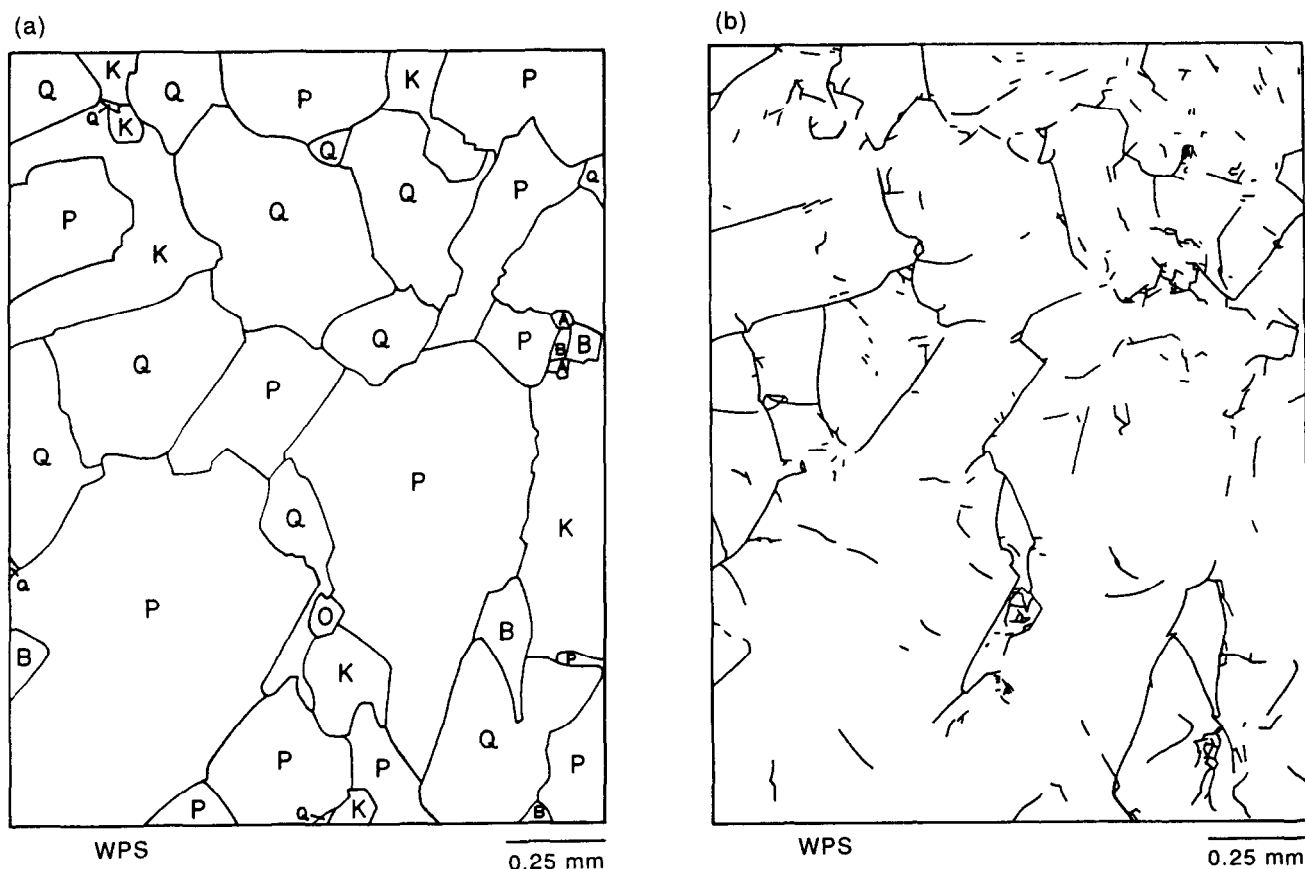(b)

WPS   0.25 mm

Fig. 2. (a) Mineral, and (b) microcrack maps of the unstressed sample WPS; cylinder axis is horizontal. (c) Mineral, and (d) microcrack maps of the area around the fracture tip at A-1. The subzone boundaries of A-1 are marked in (c), and the rupture is indicated by the heavy black line in (d). Mineral abbreviations: Q—quartz; P—plagioclase; K—microcline/orthoclase; B—biotite; M—muscovite; O—opaque mineral, usually magnetite; A—apatite; Z—zircon.

site on the plagioclase. In detail, though, at least minor replacement of the plagioclase has occurred along the boundary with the K-feldspar. The plagioclase core and K-feldspar mantle are in crystallographic continuity. Westerly granite also has been subjected to late-stage igneous and hydrothermal alteration processes. Plagioclase is the most obviously affected; it contains a variety of patchy replacement minerals such as calcite and muscovite along with many healed and sealed fractures. The centers of the more heavily sericitized plagioclase crystals are dark and grainy. Quartz also contains numerous healed fractures, as evidenced by bands of fluid inclusions.

Microcracks in both the stressed and unstressed samples are typically shorter than the average grain size of about 0.75 mm, as illustrated by the crack-length distributions in Fig. 3. The longest intragranular crack in the undeformed sample WPS measures 270 μm and the longest grain-boundary crack measures 350 μm. The maximum crack lengths in the stressed samples are 500 μm for intragranular cracks and 590 μm for grain-boundary cracks. Most microcracks are confined to the interior or edge of a single crystal, and the longest cracks follow the margins of elongate crystals, cleavage planes within biotite and feldspar, and simple twin planes in plagioclase. The few cracks that are continuous across a grain boundary generally have markedly different orientations on either side. Many other cracks in adjoining

crystals terminate close to each other at a grain boundary but are not connected in the field of view.

Total crack densities

Microcrack data for the 10 images are summarized in Table 1. The total crack density in the undeformed sample WPS, expressed in terms of crack length per unit area of granite, is 7.5 mm mm^{-2}. The three images (A-3, A-4, C-1) that are located well away from the shear fracture (far field) have very similar total densities of 14.2–14.6 mm mm^{-2}, which is nearly double the value for the undeformed sample. Moving towards the fracture from the sides or the front, crack densities increase sharply, such that the overall densities in images A-2 and B-1 are about three times the far-field value. Crack densities of the subdivided images are presented in Fig. 4. The highest crack densities in the process zone occur directly in front of the fracture tip. The narrow zone encompassing the fracture tip in A-1 has a density of at least 82.1 mm mm^{-2}, which is an order of magnitude larger than the density of the undeformed sample. The zone I portions of images A-1, B-1, and A-2, which are situated on the dilational side of the shear or its extension (Fig. 1), have 11–35% higher crack densities than their zone III counterparts on the compressional side (Fig. 4).

Crack-density profiles extending out in front and to

(c)

A-1

0.25 mm

(d)

A-1

0.25 mm
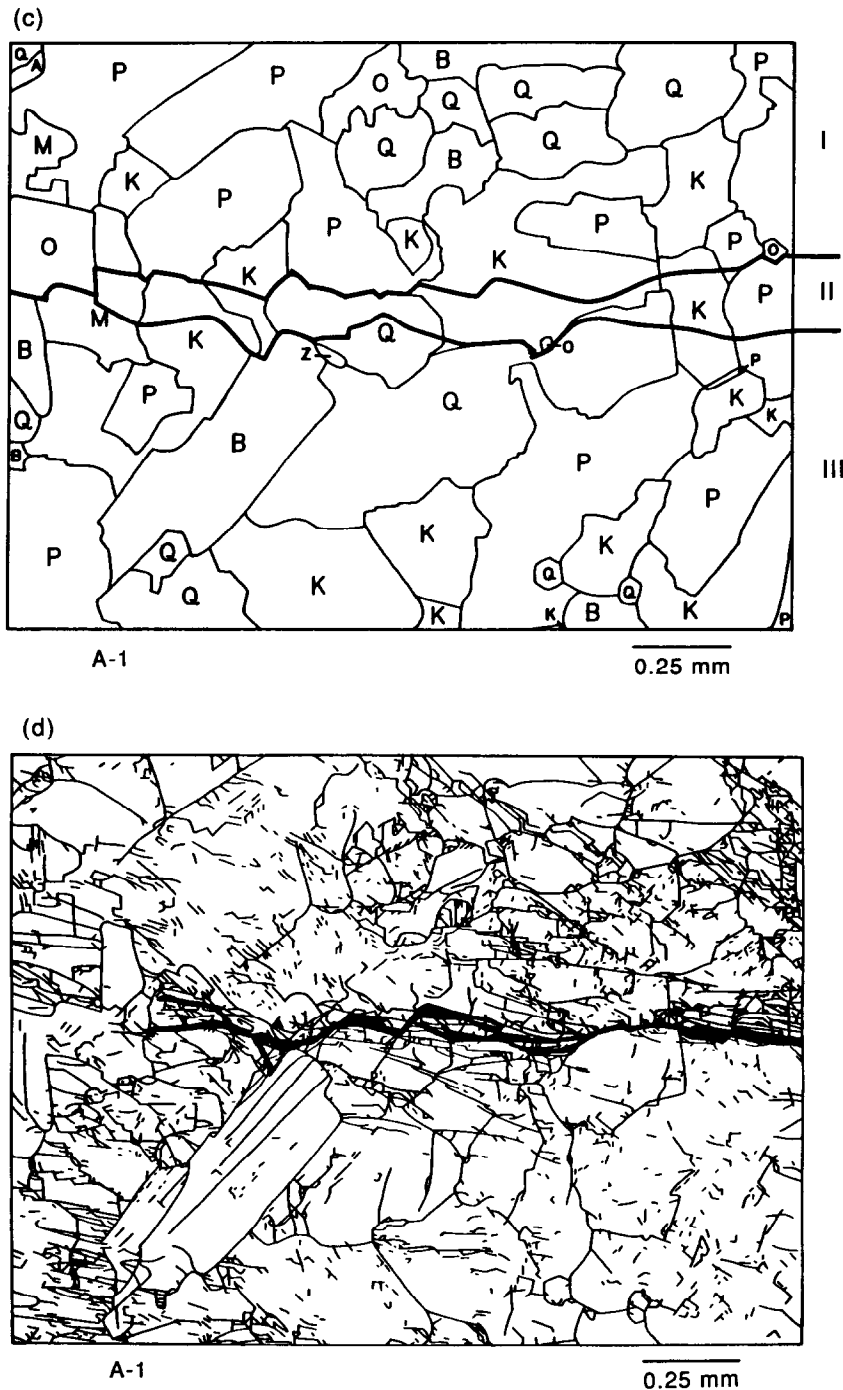
Fig. 2.   *Continued.*

the sides of the shear (Fig. 5) illustrate the rapid drop-off in microcrack density with increasing distance from the fault. Crack densities may actually be reduced to the background, far-field levels at somewhat shorter distances from the fault than indicated in the figures, because of the lack of quantitative data at those intermediate distances. In the thin sections, cracking intensity becomes visibly greater beginning about 10 mm in front and 18 mm to the side of the fault. In Fig. 5 such distances correspond to roughly 25–35% increases in crack density over background levels, which may be a reasonable threshold level for visually perceptible change. The curves in Figs. 5(a) & (b) are thus at least

qualitatively consistent with microcrack profiles in the sample.

The measured lengths of cracked grain boundaries are listed in Table 1, but because of the sample-to-sample variability in total grain-boundary length, comparisons are made here using percentages. Roughly 60% of the grain boundaries in the starting material are cracked, and they contribute nearly half (48%) of the total crack length in that sample. The proportion of grain boundaries that are cracked increases relatively regularly with decreasing distance from the shear fracture, and the highest percentages of 77–79% are found in A-1, A-2, and B-1. This suggests that there is a roughly 80% limit
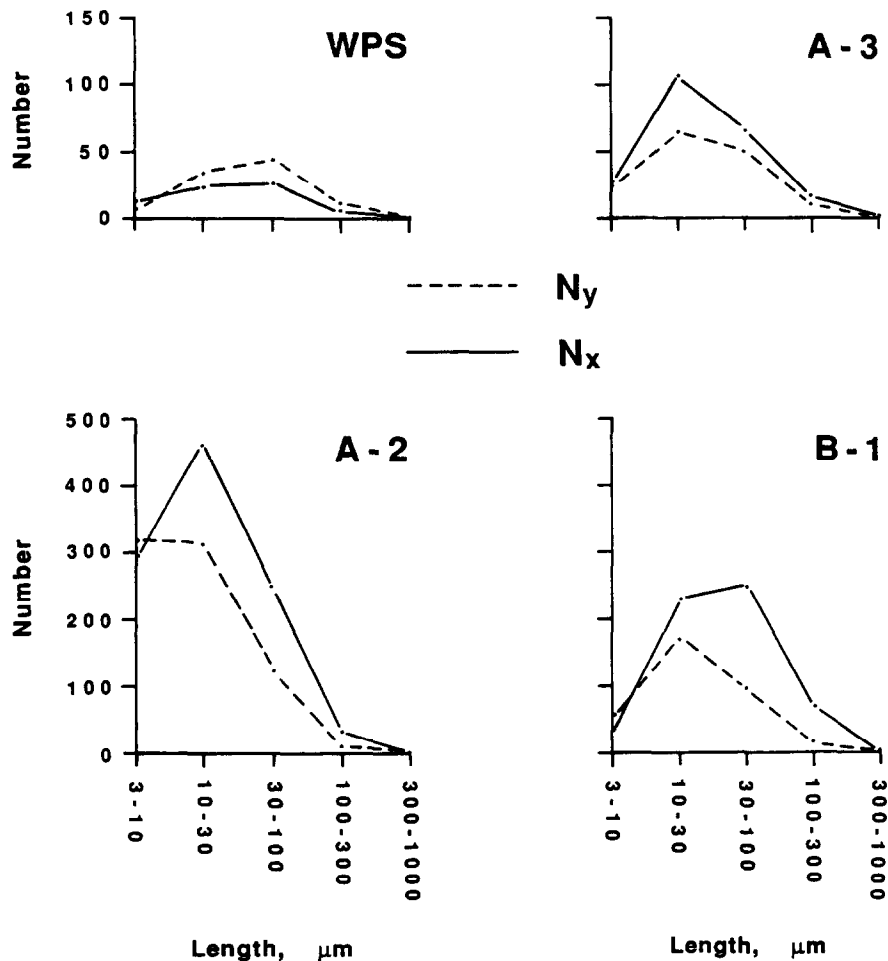
Fig. 3. Crack-length distributions in four representative images: undeformed sample WPS, far-field image A-3, process-zone image A-2, and image B-1 adjacent to the shear fracture. The crack numbers are separated into two groups by orientation: N_x—those cracks oriented within 45° of the cylinder axis ($-45°$ to 45°), and N_y—those cracks making angles larger than 45° to the cylinder axis (46°to 90° and $-46°$ to $-90°$).

Table 1. Microcrack data

Image	Area (mm²)	Total no. cracks measured	Overall crack densities [Length (mm) per mm² granite]			Intragranular crack densities [Length (mm) per mm² mineral]		
			Intragran. cracks	Grn.-Bound. cracks	Total	Quartz	Plag	Kspr
WPS	3.00	497	3.9	3.6	7.5	6.5	2.6	2.6
A-1	3.00	3211	28.9	6.9	35.8	29.7	29.0	31.8
A-2	3.00	5430	37.2	5.9	43.1	33.7	36.8	43.7
A-3	3.00	1113	9.4	4.8	14.2	16.6	6.5	6.1
A-4	3.00	930	9.5	5.1	14.6	12.4	6.8	8.1
A-5	3.00	2741	21.2	6.2	27.5	23.4	22.2	20.7
B-1	2.62	2413	33.9	5.7	39.6	34.5	31.0	37.7
B-2	3.00	2610	26.2	5.3	31.5	24.9	25.5	34.0
B-3	3.00	1871	19.7	4.2	23.9	18.1	20.2	24.3
C-1	3.00	1504	9.3	5.0	14.3	11.7	8.6	9.7

to the percentage of grain boundaries that will be cracked, at least outside the crushed zone of the rupture. Grain-boundary cracks contribute about 33% of the total crack length at the far-field locations in the deformed sample, less than 20% of the crack length near the shear fracture, and only 7–8% in the central zones (II) of the images A-1 and A-2. The great increases in crack density in the process zone and along the shear

fracture, therefore, are principally attributable to the formation of new intragranular cracks.

Crack densities—by mineral

Grain-boundary cracking is strongly correlated with mineralogy (Table 2). In the undeformed sample, grain boundaries involving quartz are the ones most com-

CRACK DENSITIES ALONG FRACTURE
(mm/mm² granite)

Dilational Quadrant

| 4 0 | 3 7 | 4 2 |

| 5 5 | 8 2 | |

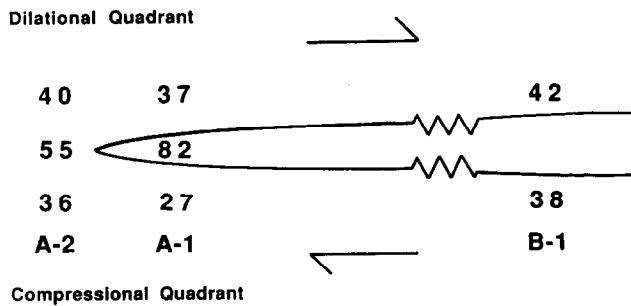| 3 6 | 2 7 | 3 8 |

| A-2 | A-1 | B-1 |

Compressional Quadrant

Fig. 4. Normalized total crack densities (length per unit area of granite) along the shear fracture, obtained from the subzones of images A-1, A-2, and B-1. Subzone areas are listed in Fig. 1. Total number of microcracks measured in each subzone. A-1 (I = 1498, II = 450, III = 1263); A-2 (I = 1706, II = 2316, III = 1408); B-1 (I = 1323, III = 1090).

monly cracked. The boundaries between adjoining quartz crystals are 90% cracked, and 70–75% of quartz–feldspar boundaries are cracked. In contrast, just over 10% of the boundaries between plagioclase and K-feldspar have open cracks. The nine images in the deformed sample are averaged together in Table 2. All of the percentages are higher in the deformed sample, to the extent that nearly all grain boundaries involving quartz are cracked. Yet, even though cracking of K-feldspar–plagioclase boundaries has increased considerably in the deformed sample, more than half of these boundaries remain uncracked.

Intragranular cracks in the unstressed sample WPS are also concentrated in quartz (Table 1), which contains about 2.5 times the normalized intragranular-crack length of either feldspar. The crack densities of all three minerals increase in the stressed sample, but at a greater rate in the feldspars than in quartz. Intragranular cracks at the three far-field locations are somewhat variably distributed: quartz to feldspar ratios in A-3 are almost the same as in the unstressed sample, but for C-1 intragranular crack densities in quartz are only 20–40% higher than in feldspar. Among the six locations nearer the shear fracture, the densities of cracking within quartz and plagioclase are roughly comparable, with quartz being more highly cracked in some images and plagioclase in others. For those same six images, intra-granular crack densities in K-feldspar average 17% higher than in quartz and plagioclase. The largest increase in intragranular crack length over the initial value in Table 1 is about 500% for quartz, 1400% for plagioclase, and 1700% for K-feldspar. Separate crystals of a given mineral in any one image can have widely varying crack densities.

Microcrack orientations

The microcrack orientations vary among the different images, as illustrated by the histograms in Fig. 6. The majority of the crack length in the undeformed sample
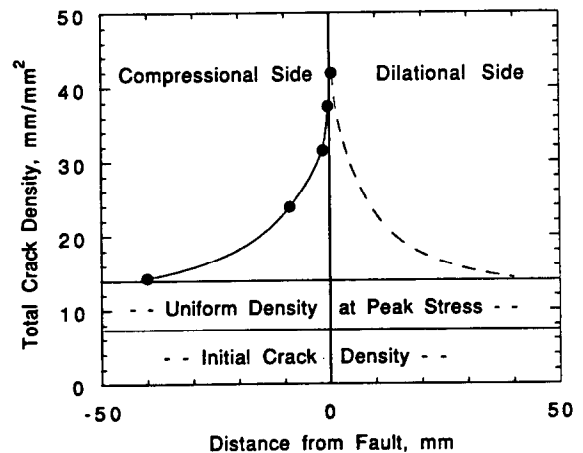
a)
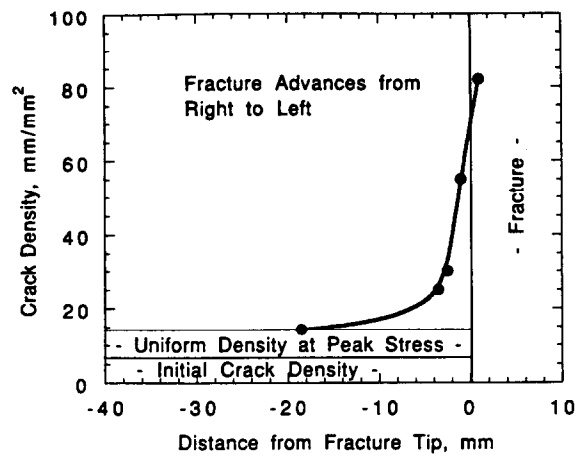
Fig. 5. Plots of total crack density relative to distance from fault for the images located (a) in front and (b) to the sides of the fault. In (b) an exponential curve $D = ae^{-by}$ was fit to the data points on the compressional side, where $a = 23.4$ mm mm^{-2} and $b = 0.109$ mm^{-1}, considering only the crack density in excess of the background damage. Crack densities probably also decrease exponentially with increasing distance from the shear fracture on the dilational side, as suggested by the dashed line, but density data are only available adjacent to the fracture.

b)

Table 2. Percent cracked grain boundaries

Minerals at boundary	Undeformed sample (WPS)	Stressed sample (9 images)
Qtz–Qtz	90%	97%
Qtz–Plag	72%	90%
Qtz–Kspr	76%	90%
Plag–Plag	29%	68%
Kspr–Kspr	60%	66%
Plag–Kspr	12%	41%

(Fig. 6a) occupies a relatively wide angular range centered around ±90°, but with a spike at 50–60° that consists principally of cracked grain boundaries and that corresponds to the alignment of the tabular crystals. In contrast, the far-field sample A-3 has a modest preferred
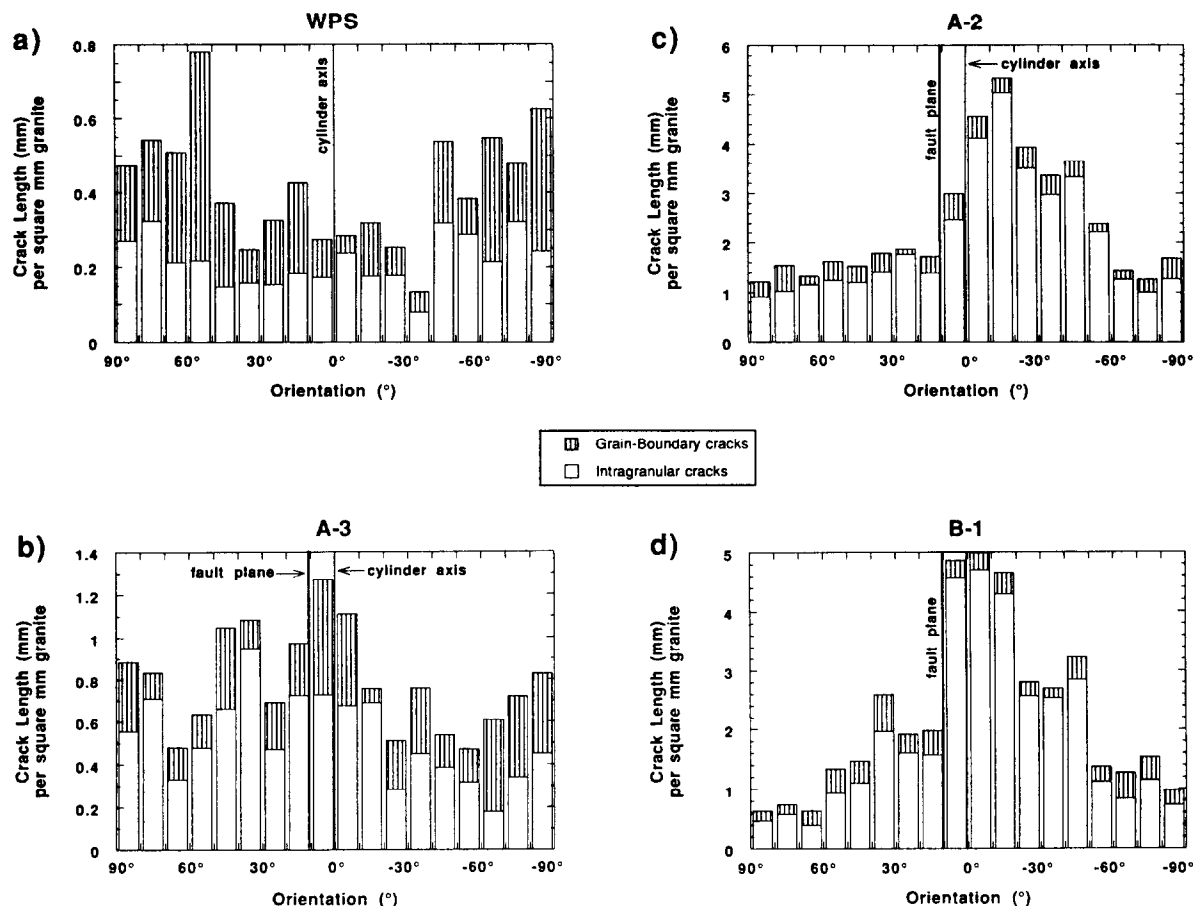
Fig. 6. Histograms of total crack density (subdivided into intragranular and grain-boundary crack lengths) relative to orientation in 10° intervals (see Fig. 1), for (a) unstressed sample WPS, (b) far-field image A-3, (c) process zone image A-2, and (d) image B-1 straddling the shear fracture.

Table 3. Length of fault following intragranular and grain-boundary paths

Fault path	Length (mm)			
Grain boundaries	16.9			
		Expected intragranular fault length based on		
Intragranular cracks:		mineral proportions		(mm)
Quartz	6.3	Quartz		14.2
Plagioclase	24.2	Plagioclase		22.9
K-Feldspar	13.8	K-feldspar		10.9
Biotite	6.5	Biotite		2.5
Other	0.3	Other		0.6
Sum	51.1	Sum		51.1
Total	68.0			

orientation approximately parallel to the cylinder axis (Fig. 6b); this distribution is typical of the far-field samples. The microcracks in the process zone have yet another preferred orientation, centered at −30° and with a maximum at −10° to 20° (Fig. 6c). Microcracks surrounding the shear fracture at B-1 are principally oriented in the range 10° to 20°, with a more rapid drop-off on the (+)-angle side than on the (−)-angle side (Fig. 6d). Microcrack counts for these same four images (Fig. 3) are separated into two groups by orientation: those making angles of less than 45° (N_x) and more than 45° (N_y) to the cylinder axis. In WPS N_y exceeds N_x for all

size categories except the smallest, whereas the reverse is true for the three images from the stressed sample.

Fault path

The nearly 70 mm of fault contained in thin sections A and B were examined to determine the relative amounts of intragranular and grain-boundary cracks that were incorporated into the fault. Three-fourths of the examined fault length follows intragranular cracks and one-fourth follows grain boundaries (Table 3). The intragranular fault length is concentrated in the feld-

spars, principally plagioclase. The right-hand column of Table 3 shows the calculated distribution of the 51.1 mm of fault length that passes within crystals, assuming that the lengths reflect the mineral proportions reported by Moore (1993) for the granite. The fault cuts through K-feldspar and plagioclase crystals to a slightly greater extent than predicted from their abundances. The fault passes through quartz crystals for only about half the calculated length and through biotite crystals for about twice the calculated length.

DISCUSSION

Comparison to other studies

Wong (1985) calculated total crack lengths in samples of stressed and unstressed Westerly granite from the direct measurements of Hadley (1986) and the stereological data of Tapponnier & Brace (1976) and Fredrich & Wong (1976). The 7.5 mm mm^{-2} crack density obtained for undeformed Westerly granite in this study falls within the 6.6–7.7 mm mm^{-2} range for unstressed Westerly granite reported by Wong (1985). The addition of cracks less than 3 μm in length would raise the 7.5 value by about 5% (Wong 1985). On the other hand, our examined image of undeformed Westerly granite is somewhat enriched in quartz compared to the average rock composition (Moore 1993). Because of the strong association of microcracks with quartz in the undeformed rock, adjusting the mineral proportions to the average value would reduce the crack density by 5.5%. These two corrections effectively cancel each other, leaving the crack density at 7.5 mm mm^{-2}. Wong (1985) calculated crack densities of 12.1–12.8 mm mm^{-2} for the same sample of Westerly granite taken to about 95% of its peak strength at 50 MPa confining pressure. The slightly higher range of 14.2–14.6 mm mm^{-2} for the three far-field images is consistent with the fact that the sample in this study was stressed up to and beyond peak strength to failure.

Fredrich & Wong (1986) distinguished between grain-boundary and intragranular cracks in their study of microcrack populations. Their sample of undeformed Westerly granite contained an essentially 50–50 split between the two types of cracks, which is almost identical to the division of cracks in WPS (Table 1). This close correspondence is significant, because Fredrich & Wong (1986) worked on so-called 'crack' sections, which are about three times the thickness of the standard polished sections used in this study. If preparation of the thinner section leads to increased cracking during handling, as commonly presumed, the relatively weak grain boundaries should be the most susceptible to damage.

As an additional test of the effect of sample thickness on the crack data, an image was also obtained from a 'crack' section of undeformed Westerly granite that had been used in a previous study (Moore *et al.* 1987). Because of the difficulties encountered in distinguishing between the feldspars in the crack section, only the total

crack length and crack orientations were determined. The image from the 'crack' section has a crack density of 7.2 mm mm^{-2}, which is 4% lower than the value for WPS. In contrast to the feldspars, the quartz content of the 'crack'-section image could easily be determined. The image contains 25% quartz, which is essentially identical to the average composition of the Westerly granite stock and lower than the 31% quartz content of WPS. The difference in quartz content easily accounts for the slight differences in crack density between the two undeformed samples. The microcracks in the 'crack' section also have a preferred orientation similar to that shown in Fig. 6(a). These results indicate that thin section preparation techniques did not noticeably affect the crack data reported in this study.

Hadley (1976) concluded that typical lengths of individual microcracks in Westerly granite are substantially less than the grain size, but she noted a shift to longer cracks in the sample stressed almost to peak strength. The maximum crack lengths measured by Hadley (1976) were 565 μm in the stressed sample and 275 μm in the undeformed sample, which are very similar to the maxima of 500–590 μm and 275–350 μm, respectively, found in this study. The 350 μm-long grain-boundary crack in WPS is somewhat long compared to Hadley's results, but WPS also has the largest average crystal size of the 10 examined images (Moore 1993).

The granite stock used in this study has a modest crystal-shape alignment (flow structure) and a more pronounced alignment of microcracks. Based on the shape of the quarried blocks—305 mm × 305 mm base, 280 mm high—the microcracks are inferred to be oriented parallel to the horizontal plane (i.e. ground surface) at the quarry. Quarried granites commonly break more easily in one direction than the others; this plane of easiest splitting is called the 'rift' plane (Dale 1923). From his extensive studies of granite quarries in New England, Dale (1923) determined that the rift plane is parallel to and caused by a preferred orientation of microcracks. His conclusion has since been corroborated by Douglas & Voight (1969), Peng & Johnson (1972) and Simmons *et al.* (1975). The rift plane is horizontal in Westerly granite (Dale 1923), as concluded in this study. The inclined mineral fabric visible in Figs. 2(a) & (c) has also been described by Dale (1923) and Tullis & Yund (1977). Both fabric elements may be general characteristics of this rock.

The links between mineralogy and microcracking in undeformed granite have not been considered in detail in previous studies, but there is some suggestion that the cracks are concentrated in and around quartz (e.g. Dale 1923, Peng & Johnson 1972, Sprunt & Brace 1974), as reported here. For stressed samples, Tapponnier & Brace (1976) indicated that, in a sample of Westerly granite stressed almost to failure, K-feldspar and quartz had somewhat higher crack densities than plagioclase. Tullis & Yund (1977) found that intragranular cracking in the feldspars exceeded that in quartz in samples of Westerly granite stressed to failure at room temperature. These results indicate somewhat variable re-

sponses of quartz and plagioclase to stress, but K-feldspar consistently is highly cracked in stressed samples. Kranz (1979) described large crystal-to-crystal differences in crack density that were also observed in this study. Crack densities in heated samples may not be wholly applicable here, but Fredrich & Wong (1986) did find that upon heating, quartz–feldspar grain boundaries in Westerly granite cracked more readily than feldspar–feldspar grain boundaries, presumably reflecting the relative contrast in their coefficients of thermal expansion. They also found slightly higher intragranular crack densities in K-feldspar than in plagioclase. In samples of Westerly granite heated to 150°C and also stressed at 250 MPa confining pressure, crack densities were somewhat higher in K-feldspar than in the other minerals (Wong 1982a).

Mineralogical controls on cracking

Westerly granite and other granitic rocks have a long and complex history of cracking and subsequent healing and sealing processes (Sprunt & Nur 1979). The crack density in Westerly granite has probably changed dramatically over time, along with the distribution of microcracks among the different minerals. For instance, cathodoluminescence studies reveal a much higher density of healed cracks in feldspar than in quartz (Sprunt & Nur 1979), although the open cracks at present are concentrated in quartz. Many of these early-formed cracks may have been healed or sealed as a result of the movement through the granite of the hydrothermal fluids that also affected the plagioclase. The present microcrack population in Westerly granite may be strongly influenced by the pressure decrease attending uplift and unroofing of the granite pluton. The horizontal rift plane of Westerly granite (Dale 1923) suggests that its crack distribution is caused by the removal of overburden. The concentration of cracking in and around quartz in the unstressed sample may be a function of that mineral's relatively large compressibility (e.g. Sprunt & Brace 1974, Kranz 1983), which would cause a marked response of quartz to the reduction in pressure. Joint sets produced by unloading generally develop at burial depths of less than 0.5 km (Engelder 1987).

With the application of stress, relatively weak spots in the rock might be expected to crack preferentially. Grain boundaries are obvious weak sites in the rock, and the proportion of cracked grain boundaries increased overall in the stressed sample. The lesser degree of cracking along K-feldspar–plagioclase boundaries is due in large part to the commonly occurring K-feldspar mantles over plagioclase. Because the K-feldspar overgrowth is in crystallographic continuity with the plagioclase core, the contact between the two minerals will be much stronger than is characteristic for grain boundaries. These mantled K-feldspar–plagioclase boundaries are consistently the ones least likely to be cracked, and they are the major cause of the observed 80% ceiling on grain-boundary cracking in the stressed sample. The remaining uncracked grain boundaries consist principally of ones that have been sealed by mineral deposits and others that are unfavorably oriented relative to the loading direction.

The slight concentration of cracking in K-feldspar close to the shear fracture is closely related to the two perfect cleavages in that mineral. Wong (1982a) calculated that of the three major minerals in Westerly granite, microcline is the most anisotropic with respect to its elastic properties, and in appropriate orientations it will attain the largest maximum stress. Plagioclase also has one perfect and one good cleavage plane, and it should behave similarly to microcline. The extensive hydrothermal alteration of some plagioclase crystals may interfere with the development of long cleavage cracks, however, because the plagioclase structure will be interrupted in places by replacement minerals that could provide a barrier to crack propagation. According to Wong (1982a), microcracking in plagioclase in Westerly granite is more closely associated with pores resulting from the hydrothermal alteration than with cleavage planes. The observed crystal-to-crystal variations in crack density for a given mineral probably reflect differences in crystallographic orientation relative to the stress field (e.g. Wong 1982a).

Microcrack and stress orientations

Many previous studies have demonstrated that microcracks induced during uniaxial or triaxial loading of granitic rock are principally tensile cracks (e.g. Hadley 1976, Tapponnier & Brace 1976, Kranz 1979, Wong 1982a, Howarth 1987). If that is the case, two separate sets of tensile cracks should be present in the laboratory sample, corresponding to the two stages of acoustic emission described by Lockner *et al.* (1992a). The sample was loaded parallel to the cylinder axis; thus, tensile cracks formed during the early, distributed stage of acoustic emission should have a roughly axial orientation, as illustrated in Fig. 7(a). Once the shear fracture forms, the microcracking that is concentrated in the process zone will be most highly influenced by the stress fields generated by the fracture itself, as indicated schematically in Fig. 7(b). The expected amount of rotation of the principal stress axes under the influence of the shear fracture is shown in Fig. 8, which plots the orientation of the least compressive stress axis along a line perpendicular to the fracture and 4.5 mm ahead of the fracture tip. The modelling of the stress field from which Fig. 8 is derived uses the observed fault-propagation direction of 10° to the cylinder axis and the stress state in the sample at the time of failure; this modelling is detailed in the next section. The plot suggests a rotation of as much as −20° in a region 5–10 mm on either side of the shear fracture, with the rotation being somewhat greater on the dilational side of the fracture.

The far-field images contain the cracks already present in the undeformed rock combined with those added during initial loading of the sample. The images in the process zone contain all the cracks of the far-field areas
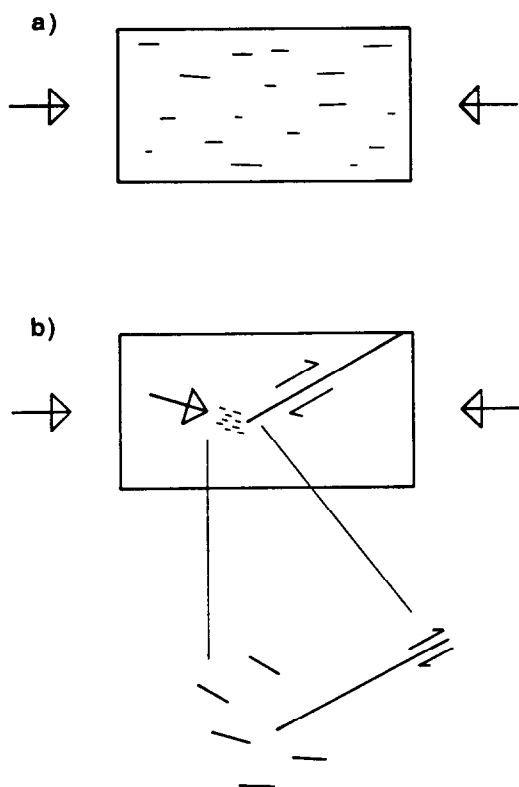
a)

b)

Fig. 7. Sketches of expected orientations of tensile cracks formed: (a) during initial loading of the cylinder, and (b) in the process zone in front of the fault. Crack orientations around the fault are estimated from fig. 8.6c of Pollard & Segall (1987).

Orientation of Least Compressive Stress

Fig. 8. Predicted rotation of stress axes in front of the shear fracture, calculated using the stress equations presented by Pollard & Segall (1987), in which the fault is inclined 10° to the remote principal stress field (loading direction of experiment). Details of the modelling are presented in the section on stress field approximation. Rotations of the principal stresses of up to 20° from the remote stress directions are predicted, with maximum rotation occurring slightly on the dilational side of the shear fracture.

plus those cracks induced by the advancing fracture. A rough way to isolate the pre-failure cracking would be to subtract the histogram for the undeformed sample from that of a far-field image, that is, subtract Fig. 6(a) from (b). In turn, cracking associated with the process zone can be isolated by subtracting a far-field histogram from one for a process-zone image, such as subtracting Fig. 6(b) from (c).

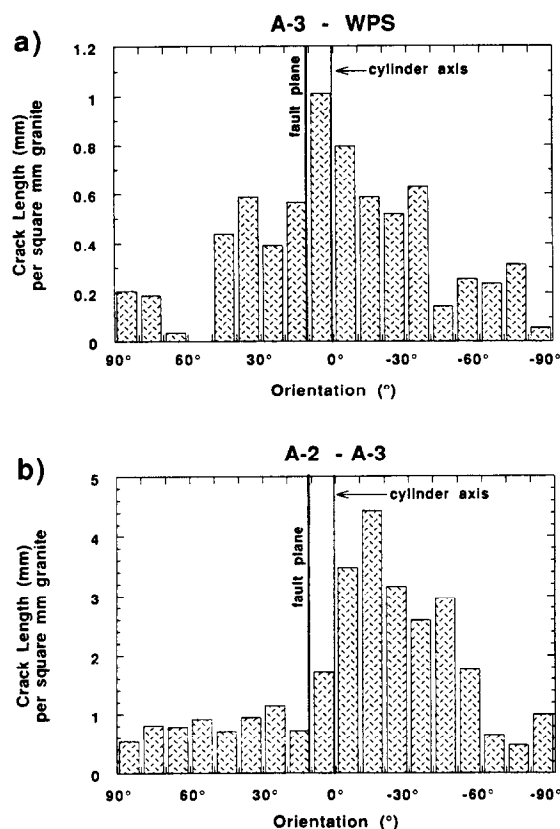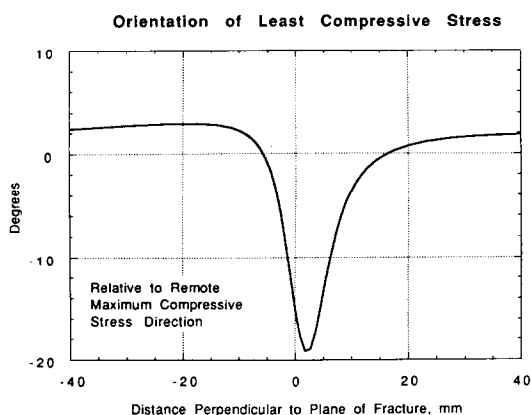As mentioned previously, thin sections from both the

a)

b)

Fig. 9. Orientations of microcracks formed: (a) during initial loading of the cylinder, obtained by subtracting the histogram for the undeformed sample WPS from that for the far-field image A-3, and (b) in the process zone, obtained by subtracting the histogram for A-3 from that for process-zone image A-2.

small and large cylinders contain the vertical axis of the granite block, but the horizontal direction being viewed may differ. However, the major microcrack fabric in the granite block is horizontal, and it will be centered around ±90° in thin sections from both the stressed and unstressed samples, whatever the viewing direction. Westerly granite does contain the inclined mineral fabric, which influences the distribution of grain-boundary cracking. The orientation of this fabric in a given thin section will vary with the direction that it is cut by the section. The tabular crystals contributing to the fabric nevertheless have similar orientations of 50–60° in the thin sections from both cylinders (Figs. 2a & c; see also Moore 1993), which suggests that the sections can be freely compared.

The orientations of microcracks generated during the different stages of cracking in the laboratory sample (Fig. 9), determined by subtracting histograms as described above, are consistent with those of the tensile cracks illustrated in Fig. 7. Microcracks formed during the initial loading of the sample (Fig. 9a) are roughly parallel to the cylinder axis, with some spread of orientations reflecting crystallographic influences. For example, a complex crack oriented at 0° overall in a feldspar may consist of a stairstep arrangement of smaller cracks that follow the cleavages in the mineral. Similarly, Wong (1982a) calculated that the maximum compression direction in feldspars can rotate towards
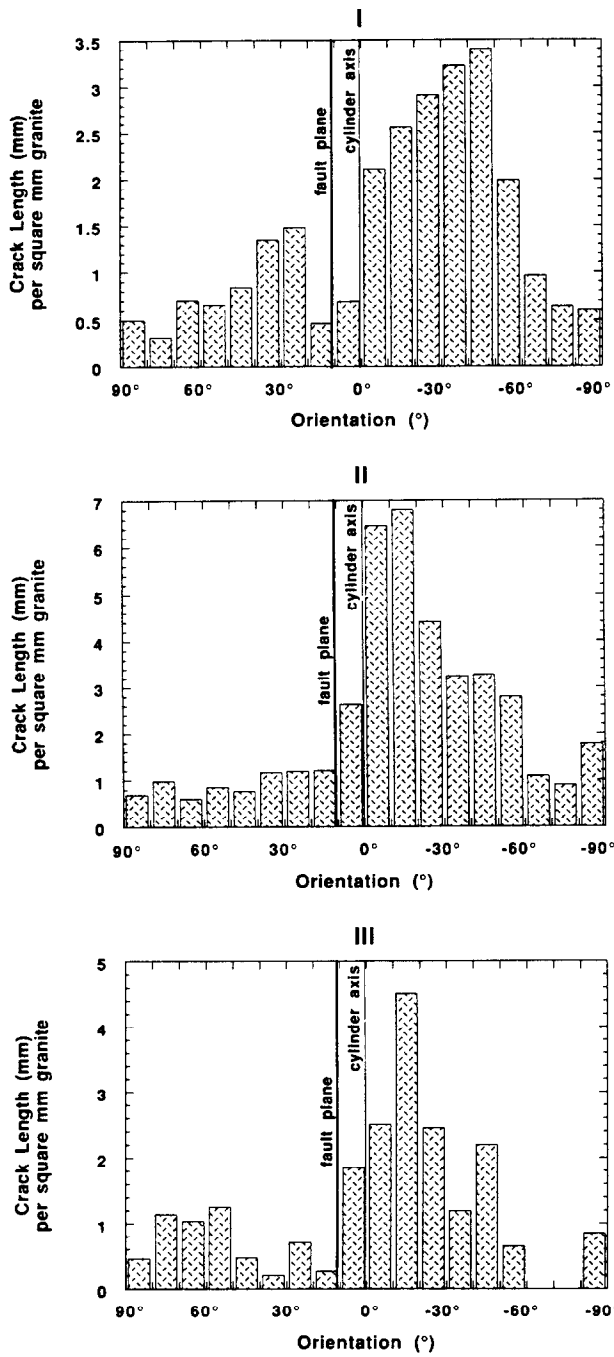
Fig. 10. Microcracks generated in different parts of the process zone, obtained by subtracting the histogram for A-3 from that for each subzone of image A-2.

the nearest cleavage plane by up to 10°. Microcracks generated in the process zone (Fig. 9b) are rotated away from the cylinder axis in the direction indicated in Figs. 7(b) and 8.

The preferred orientations of microcracks in different parts of the process zone are also generally consistent with the local stress field associated with the shear fracture (Fig. 8). If the subsections of image A-2 are considered separately (Fig. 10), the cracks in zone I on the dilational side of the shear make larger angles to the shear than those in zone III on the compressional side,
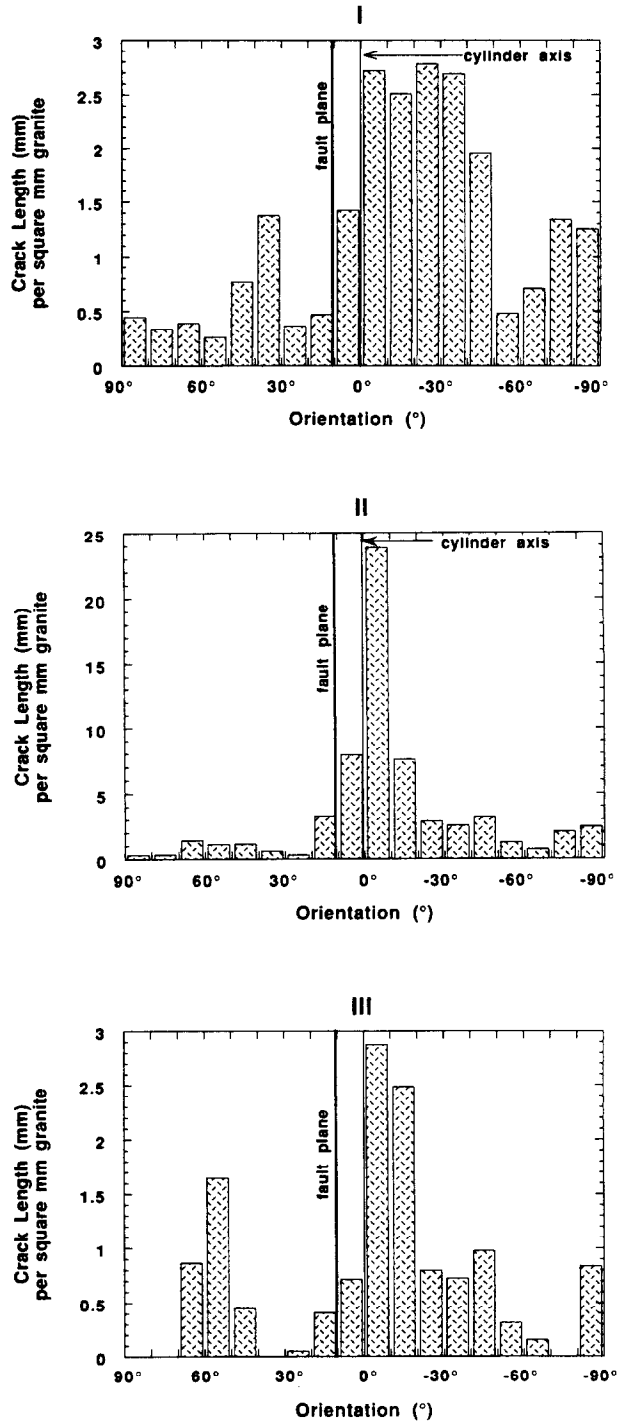
Fig. 11. Histograms of microcrack density obtained by subtracting A-3 from the subzones of A-1.

consistent with the expected relative orientations in Fig. 8. However, the microcracks in zone II, directly in front of the fracture tip, trend at slightly smaller angles overall than those in either zone I or III. This shift in orientation is not due to a lack of cracks at larger angles in zone II. For the orientation range −20° to −60°, zone II contains the same crack length as zone I and more than III. The difference is that zone II contains even more cracks in the range 0° to −20° than zones I and III. Similar relations are shown for the subsections of image A-1 (Fig. 11), from

which the far-field crack population has been removed. Zones I and III of A-1 principally consist of microcracks that formed in the previous position of the process zone, and the relative orientations of cracks in those two zones are consistent with the equivalent parts of A-2. Zone II of A-1 contains many new cracks oriented at a small angle to the shear fracture.

The relative time of formation of the smaller-angle microcracks in zones II of A-1 and A-2 cannot yet be demonstrated, but their presence is consistent with a possible two-stage sequence to fracture propagation. During the first stage, predominantly tensile cracks form throughout the process zone. These sub-parallel cracks must become connected for the fracture tip to advance, and in the second stage smaller-angle linking cracks develop between those tensile cracks positioned directly in front of the fracture tip. Eventually a through-going zone of damage is created, leading to a loss of cohesion and advance of the rupture. Cox & Scholz (1988) described a similar sequence of microcracking associated with propagation of a mode III fracture. The linking cracks in their samples may have had local mode II shear displacements. Consistent with their results, the linking cracks in zone II of images A-1 and A-2 are oriented similarly to R_1-type Riedel shears, although no evidence of slip along them was observed at the magnifications used. Alternatively, the linking cracks could also be a new generation of tensile cracks, which formed as a result of stress reorientations between the previously formed microcracks.

Stress field approximation

In this section we address the question of how the observed microcrack damage is related to the stress field associated with the advancing fracture front. In this experiment, the fracture has grown to nearly the full sample size so that the stress boundary conditions applied to the surface of the sample cannot properly be considered remote stresses (i.e. stresses applied outside the influence of the fracture-induced stress field). Consequently, a proper stress field analysis becomes complex and is beyond the scope of this paper. By making the following simplifying assumptions, however, we can show in a general way how microcrack damage in the process zone is related to the stress field associated with the fracture. We consider the stress field about a two-dimensional elliptical crack in a homogeneous, elastic medium. The process zone is probably better modeled as a plastic yield zone; however, this refinement will be added at a later time. We use the stress equations presented by Pollard and Segal (Pollard & Segall 1987, p. 305) and assume that the crack is closed (transmitting normal stress) but has zero friction (no shear tractions). Because the fracture propagation is dominantly mode II in the region studied, we consider pure mode II loading in our simplified modelling. To simulate the applied load, we assume that the remote maximum compressive stress σ^r_{max} is aligned with the cylinder axis. Approximately one-third of the sample cross-section was frac-

tured by the end of the experiment. By assuming that this portion of the sample supported an axial load consistent with a sliding friction of 0.75, we estimate that the remaining unfractured portion of the sample supported an axial load of approximately 544 MPa at the end of the experiment. We use this value to approximate the remote axial stress σ^r_{max}. The remote minimum compressive stress σ^r_{min} corresponds to the confining pressure (50 MPa). Then, relative to the fracture plane (half-length of 90 mm), which was inclined 10° to σ^r_{max}, we have (in MPa) $\sigma^r_{\alpha\alpha} = 529$, $\sigma^r_{\beta\beta} = 65$, and $\sigma^r_{\beta\alpha} = 84.5$, where α is the propagation direction of the fracture and β is the normal to the fracture surface. Because the fracture is closed, normal stresses are transmitted across the fracture plane. Consequently, using the nomenclature of Pollard & Segall (1987), the mode I driving stress $\Delta\sigma_I = 0$. Because the fracture is considered frictionless in our simplified model, mode II driving stress is just $\Delta\sigma_{II} = \sigma^r_{\beta\alpha}$.

As demonstrated in the previous section, the microcracks in the damage zone surrounding the advancing fracture appear to open primarily in tension. Because the overall stress state is on average compressive, the development of locally dilational stress fields must be the result of stress concentrators on the scale of the grain size or smaller in homogeneous rock (granite is clearly heterogeneous for scales less than or equal to the grain size). This represents a fundamental notion in our understanding of brittle fracture (e.g. Peng & Johnson 1972, Tapponnier & Brace 1976, Ashby & Sammis 1990, Lockner & Madden 1991, Lockner 1993). In a two-dimensional model of brittle fracture in crack arrays, Lockner & Madden (1991) found that most cracks supported stresses similar to the remote loading stresses, but the stress distribution broadened with increasing deviatoric stress until a subset of cracks moved from a compressive to a tensile stress state and began to fail in tension. This corresponded to the onset of dilatancy at 50–60% failure strength, which has been observed for many rock types. We argue that a similar condition holds in the case of a propagating shear fracture. It is unlikely that a shear fracture subjected to any significant confining pressure can reverse the sign of the minimum principal compressive stress throughout the entire damage zone. The stress singularity at the tip of a sharp fracture may produce a locally tensile stress component, but as we will show, the damage zone observed in our experiments appears to extend beyond this stress singularity into a region where remote stresses are comparable to crack-induced stresses. Furthermore, the blunting of the stress singularity due to the presence of the damage zone will further diminish the ability of the crack to develop a truly tensile stress region. Thus, we argue that the microcrack damage induced around the advancing fracture is to a large degree the result of increased deviatoric stress, just as the background damage in the sample is the result of uniformly increasing deviatoric stress.

Based on the preceding argument, we propose a damage criterion $\tau^* = c + \sigma_n \tan \phi$ based on Coulomb failure, where τ^* is the maximum shear stress on the
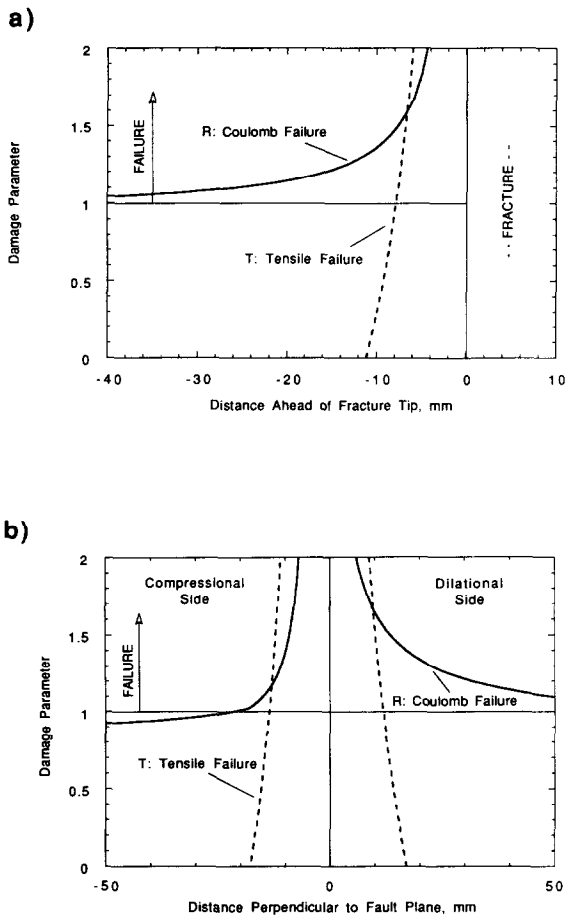
a)

b)

Fig. 12. Plots of calculated damage parameters R (Coulomb failure criterion) and T (tensile failure criterion): (a) in front, and (b) to the sides of the shear fracture. Failure occurs for values greater than unity. A noticeable increase in microcracking is predicted to occur 10–20 mm in front and on the flanks of the fracture tip, in agreement with the microcrack densities observed in thin section (Fig. 5). The Coulomb failure condition generally extends beyond the region in which the stress field induced by the fracture can reverse the ambient compressive stress state and lead to generalized tensile failure. Consequently, R appears to be a more appropriate damage parameter for conditions of overall-compressive loading.

macroscopic failure surface in a rock when subjected to normal stress σ_n, and c and ϕ are, respectively, cohesion and friction angle for the rock. The parameter $R = \tau/\tau^*$ $= \tau/(c + \sigma_n\tan\phi)$ is defined as the ratio of shear stress to peak shear stress resolved on a plane inclined at an angle θ to the maximum compressive stress direction ($\theta = \pi/4$ $- \phi/2$). Then, $R = 0$ at zero deviatoric stress and $R = 1$ at failure. As described above, we expect significant microcrack damage beginning with the onset of dilatancy ($R \approx$ 0.5). Independent fracture tests on Westerly granite at confining pressures up to 200 MPa resulted in values of c = 88 MPa and $\phi = 38°$. In Fig. 12(a) we plot R as a function of distance ahead of the fracture tip, based on the stress field for the two-dimensional plane-strain fracture subject to the boundary conditions described above. R asymptotically approaches the far-field value of 0.96. (It should be noted that this value is not well-constrained and could conceivably be much smaller.) The background microcrack damage (e.g. Fig. 5) re-

flects the uniform damage accumulated during the pre-failure period in which R was raised from approximately 0.5 to unity. The increase in R near the fracture tip indicates that the crack-induced stresses drive the surrounding rock farther and farther into the Coulomb failure region as the fracture advances. Then, according to this simplified analysis, there should be a direct correlation between increasing R and increasing micro-crack damage. The increase in R in Fig. 12(a) suggests that significant fracture-related microcrack damage should extend 10–20 mm ahead of the fracture tip. This prediction is in good agreement with the observed microcrack damage plotted in Fig 5(a).

A second damage parameter $T = \sigma_{min}/\sigma_T$, based on a tensile failure criterion, is also plotted in Fig. 12(a). In this equation, σ_{min} is the minimum compressive principal stress and σ_T is the tensile strength of the rock (σ_T $= -20$ MPa for Westerly granite). In this case, $T = 0$ represents uniaxial compression and $T = 1$ represents a condition of tensile failure. The region approximately 10 mm ahead of the fracture, where T is positive, represents the area in which fracture tip stresses are large enough to reverse the sign of the ambient minimum compressive stress. By contrast, the zone in which Coulomb failure can occur extends farther ahead of the fracture tip.

As a next step, we consider the microcrack damage that has accumulated on the flanks of the fracture. This damage should reflect the peak stress and accompanying microcracking experienced by each locality as the fracture tip approaches and then passes by. To determine this peak deformation state, we have determined the maximum value of R (and T) along lines of constant β (parallel to the fracture axis) over the interval $\alpha = -\infty$ to $+40$ mm. The results are shown in Fig. 12(b). Once again, the far-field asymptote is $R = 0.96$, and the model predicts increased microcrack damage as the fracture is approached from either side. The damage pattern is expected to be asymmetric with somewhat more damage accumulated on the dilational side of the fracture. The prediction that the damage zone should extend 10–20 mm from the fracture on the compressional side is in reasonable agreement with the observed microcrack damage (Fig. 5b). The tensile and Coulomb failure criteria predict essentially the same width to the damage zone on the compressional side of the fracture. On the dilational side, however, the Coulomb damage zone is expected to extend farther from the fracture. Unfortunately, we do not yet have the crack density data to test this prediction.

Shear fracture energy

Energy release rate $G_{\parallel}$ for mode II fracture propagation has been evaluated for laboratory samples using stress/displacement observations (Rice 1980, Wong 1982b, Lockner et al. 1991). Lockner et al. (1991) reported $G_{\parallel} = 13$ kJ m^{-2} for a faulted sample similar to the one examined in this study (Rice and Wong reported a range of 3–73 kJ m^{-2} in their studies). By using the

microcrack density measured on the flanks of the fracture in the present study (Fig. 5b), we can assess the fraction of the total energy release rate that is contributed by forming new surface area in the process zone. For two reasons the calculations will provide a lower bound to the new surface energy. Firstly, as already mentioned, the reported crack counts miss cracks below about $3\,\mu$m, although these small cracks are likely to add little to the total surface area of new cracks. Secondly, we ignore grain crushing in the narrow localized fracture zone and make no attempt to correct for this new surface area. The data for the compressive side of the fracture in Fig. 5(b) are reasonably fit by an exponential: $D = ae^{-by}$ where $a = 23.4$ mm mm^{-2} and $b = 0.109$ mm^{-1}, for which we consider only the crack density in excess of the background damage. Then, integrating along a line perpendicular to the fracture, $S = 4a/b = 860$ mm^2 mm^{-2} represents new surface area in the damage zone per unit surface area of new fault. A factor of two is included in the equation to account for the contribution of the dilational side of the damage zone, and a second factor of two is added for the fact that two new surfaces are represented by each new microcrack. Assuming that the microcrack damage is predominantly tensile, as suggested by the microcrack orientations, then $G_{\|}/G_{\rceil} \geq 860$ where $G_{\rceil}$ is mode I energy release rate. Experimental data for quartz and feldspar (Atkinson 1987, Lockner et al. 1992b) suggest that $G_{\rceil}$ falls in the range of 2–10 J m^{-2}, making $G_{\|} \geq 1.7$ to 8.6 kJ m^{-2}. Thus, the new surface area created in the damage zone may account for a significant fraction of the energy dissipated during shear fracture propagation in this experiment.

Fault propagation path

The crack density and orientation data of this study indicate that the expanse of damaged rock is asymmetrically distributed (Fig. 13) around a mode II fracture, which may have considerable influence on the local fault geometry. Theoretical calculations predict in-plane propagation of a mode II fracture (e.g. Fischer 1992), but the microcrack fabric and density variations in the process zone would tend to pull the propagating shear fracture towards the dilational quadrant. Figure 14(a) shows two small-scale examples of this tendency. Tension cracks make a relatively large angle to the long segment in the center of the photomicrograph. At either end of that segment, the shear fracture makes a small jog roughly parallel to the microcrack trends. These two jogs are short, but other, longer segments have a similar orientation. In order to counterbalance the segments that follow the microcrack fabric and retain an overall in-plane propagation path, some fault segments must head back towards the compressional side and at a larger angle to the cylinder axis than the overall fault strike. The end result is a zig-zag or sawtooth arrangement of fault segments, as illustrated in Fig. 15(a).

The final 70 mm of the shear contained in thin sections A and B (Fig. 1) were divided into segments of uniform strike. The orientations of these segments, normalized
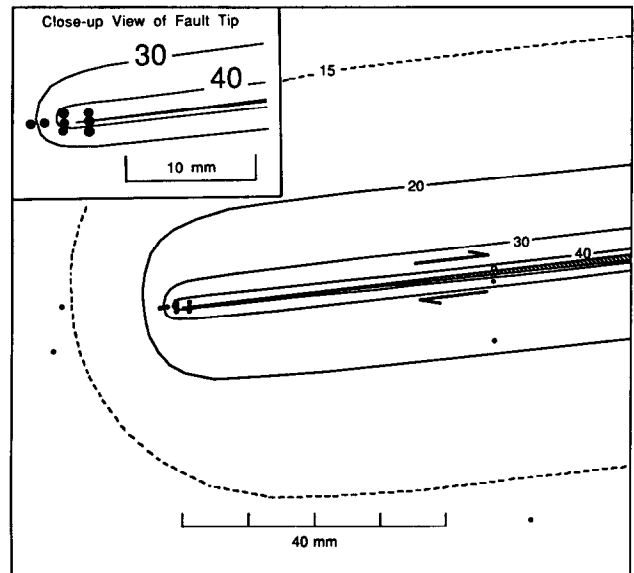

Fig. 13. Possible extent of the zone of damaged rock around the fault, indicated by estimated contours of crack density (mm mm^{-2} granite). The contours are asymmetrically distributed about the fault tip, indicating a more rapid drop-off of microcrack damage on the compressional side than on the dilational side.

to the overall fault strike, are plotted in Fig. 16. For this shear with its minimal offset, only a few segments follow the average trend of the fault, although with increasing distance from the fracture tip the segments do become longer and the angular deviations smaller (Fig. 16), as a result of fault-widening and -smoothing processes. The zig-zag pattern nevertheless is present all along the examined length. At least for small-scale faults of the type described in this study, the zig-zag geometry is built into the fault propagation system, because of the nature of microcracking in the process zone. Given an overall in-plane propagation path, the sawtooth pattern would be a second-order feature of the fault geometry. Another implication is that some controlling mechanism, such as distortion of the stress field, brings the fault back in line after one of the jogs towards the dilational side.

Recent models of the formation of shear fractures involve the growth of tensile or 'wing' cracks from suitably oriented, pre-existing flaws, which interact to form a through-going break (Horii & Nemat-Nasser 1985, Ashby & Hallam 1986). This model geometry has been observed in faulted laboratory samples of biotite-rich foliated rock (Gottschalk et al. 1990) and also in nature in places where pre-existing joint sets have been reactivated as shear faults (Segall & Pollard 1983, Granier 1985). Such faults did not extend their lengths by propagation in their own plane; rather, adjacent, overlapping shear faults became connected along the area of overlap by means of tensile cracks. The model fault envisioned by Horii & Nemat-Nasser (1985) also duplicates the sawtooth geometry of our laboratory fault (Fig. 15b), but some details of their model need to be modified to explain the growth of this type of shear fracture.

Firstly, their model assumes that the future fault plane is pre-determined in the granite cylinder. As the cylinder

is loaded to nearly peak stress, suitably inclined flaws contained within this proto-fault zone would preferentially develop wing cracks, producing a zone of high crack density prior to sample failure. However, no evidence for a pre-determined fault plane has been found in this or similarly faulted samples. The rift plane of Westerly granite is a pre-existing plane of weakness along which faulting could potentially be localized, but the rift plane was oriented perpendicular to the loading direction during the experiment. The acoustic emission measurements made on this and other samples (Lockner et al. 1992a) do not indicate the presence of localized cracking until after the fault nucleates. Instead, at the time of failure the rock as a whole apparently has a crack distribution similar to that seen in the far-field images. Similarly, other granite cylinders loaded to 99% of peak stress at various confining pressures show no evidence in thin section of the future position of the failure plane (Moore et al. 1990). Once the shear fracture nucleates, it creates its own rupture by means of the intense, predominantly intragranular cracking in the migrating process zone. Both the acoustic emission measurements (Lockner et al. 1992a) and thin-section examination of the sample demonstrate a lack of concentrated microcracking more than 10 mm or so in front of the fracture tip. Finally, if the fault reflects pre-failure microcrack concentrations, then quartz and grain boundaries should figure more prominently along its path than is the case (Table 3).

The fault segments that follow the fabric of the process zone away from the fracture plane correspond to some extent to the tensile connecting cracks of Horii & Nemat-Nasser's (1985) model (Fig. 15). In contrast to their model, however, the tensile cracks of significance here are the ones associated with the process zone, not the pre-failure axial cracks. Portions of the segments that return the shear to its overall propagation path may correspond to the pre-existing flaws of the model fault, although their purpose differs. In the model, the inclined flaws already present in the rock provide sites for the tensile cracks to form due to modest shear displacements along the flaws. In our laboratory fault suitably oriented grain boundaries and relatively weak crystals such as biotite (Kronenberg et al. 1990) may, where encountered, provide a means for the fault to return to its overall propagation path. Biotite crystals (Fig. 14) and grain boundaries do make up a slightly larger proportion of the length of returning fault segments than of the others, but more than half the path of the returning segments follows intragranular cracks in the feldspars.

The propagation of the shear fracture may be envisioned as follows. The density variations and orientations of microcracks in the process zone induce the fracture tip to propagate out-of-plane in places. As the segment length and the distance from the overall fault plane increase, continued propagation along that inclined segment may become progressively more difficult as a result of stress increases. When the fracture tip encounters a weak structure of some kind that trends

back towards the fault, a new segment following that plane of weakness will be energetically favored over continuation of the existing segment. More importantly, there may be some limiting distance away from the overall fault plane (Fig. 15a), associated with some critical stress level, beyond which a given segment cannot propagate.

The zig-zag geometric pattern of this laboratory shear fracture is analogous to the geometry of some active faults. At the southeastern termination of the San Andreas fault, for example, Bilham & Williams (1985) describe a sawtooth geometric arrangement of segments. Based on the laboratory studies, the fault-termination area should have the most obvious zig-zag pattern. Bilham & King (1989) plotted the orientation of all San Andreas fault segments with respect to the local plate motion vector. Despite the relative smoothness of the San Andreas, many obliquely oriented segments are present all along the fault trace, and the distribution of segments is similar to that in Fig. 16. King & Yielding (1984) also described a pronounced zig-zag geometry at the southwest termination of a thrust fault in Algeria. They consider the zig-zag pattern to be inherited from the network of breaks in the process zone. The progressively older fault segments to the northeast, which have larger net displacements, also have smoother traces. The process zones associated with all types of propagating faults may therefore promote the development of a zig-zag geometry.

SUMMARY AND CONCLUSIONS

(1) Open microcracks in undeformed Westerly granite are concentrated within and along the edges of quartz crystals. Alteration minerals and mineral-filled cracks provide ample indications of previous hydrothermal activity that affected both quartz and feldspars, especially plagioclase. The present crack densities therefore represent some balance between cracking and sealing processes, and the unequal distribution of cracking among the different minerals may or may not be characteristic of the granite throughout its history. The preferred orientation of the open cracks is consistent with their formation in response to unroofing of the granite pluton.

(2) Applying an axial load to a granite cylinder under confining pressure leads to increases in crack density in all minerals and reduces the proportional differences in crack density between them. Three-quarters of the examined fault length follows intragranular cracks, with only one-fourth along grain boundaries. Large crystal-to-crystal variations in crack density are a function of the orientation of the crystal lattices relative to the principal stress directions.

(3) The orientations of microcracks generated in the laboratory sample are generally consistent with tension cracks that formed under changing stress conditions, as predicted from calculations of the stress field associated with this fault. Prior to sample failure, new microcracks
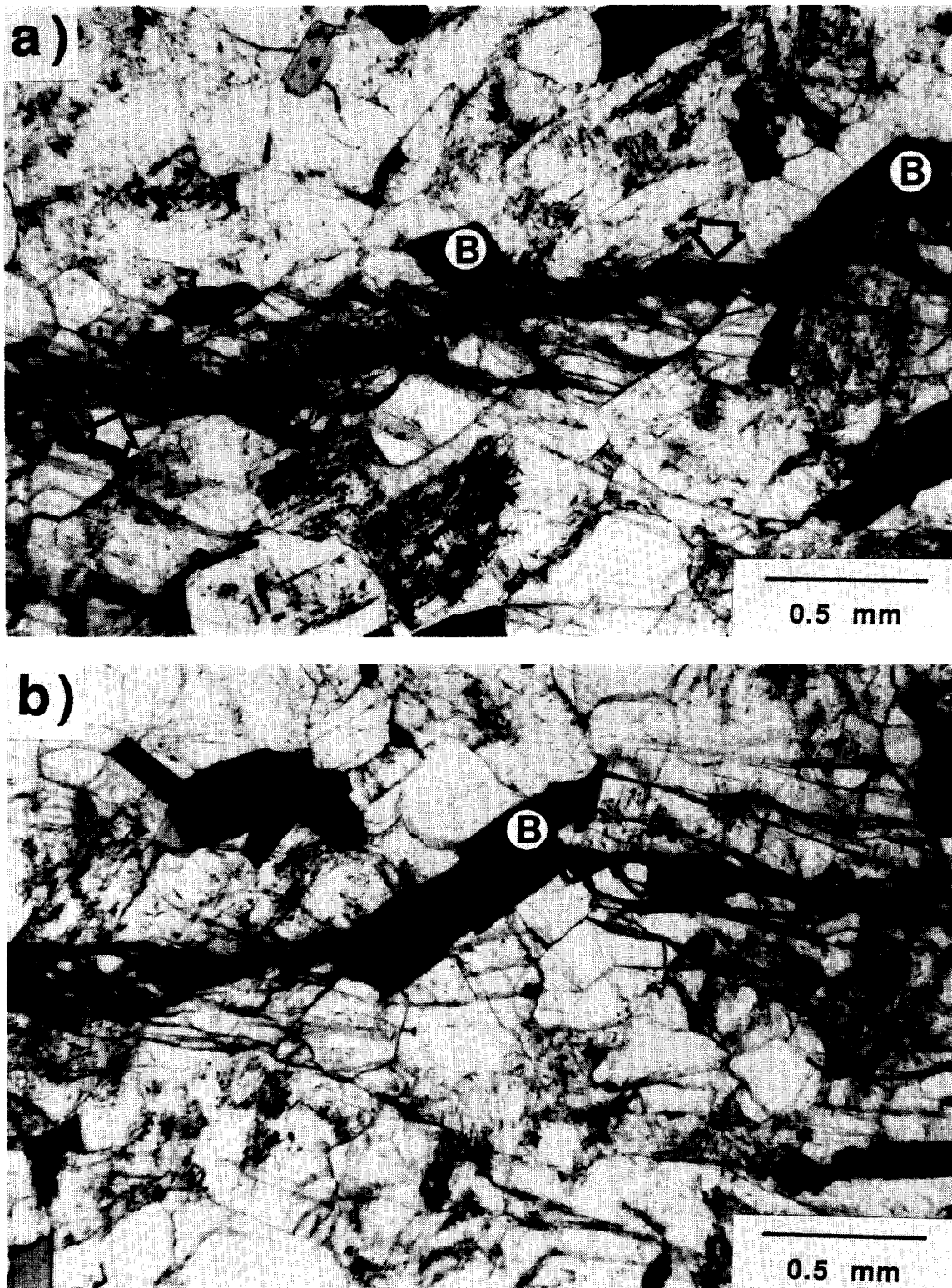
Fig. 14. Photomicrographs of zig-zag fault geometry in the shear fracture, from thin section B; plane polarized light. The propagation direction is to the left in both photos. (a) Two short segments roughly parallel to the microcrack fabric of the process zone (indicated by arrows) bound a segment that makes a large angle to the process-zone fabric. At the right, a 'returning' segment crosses a biotite crystal (B) at a small angle to the cleavage. (b) A 'returning' segment initiated at a biotite crystal. As in (a), the segment crosses the biotite at a small angle to the cleavage, then follows intragranular cracks in feldspars before terminating at a complex zone of cracking on the left side of the photo.
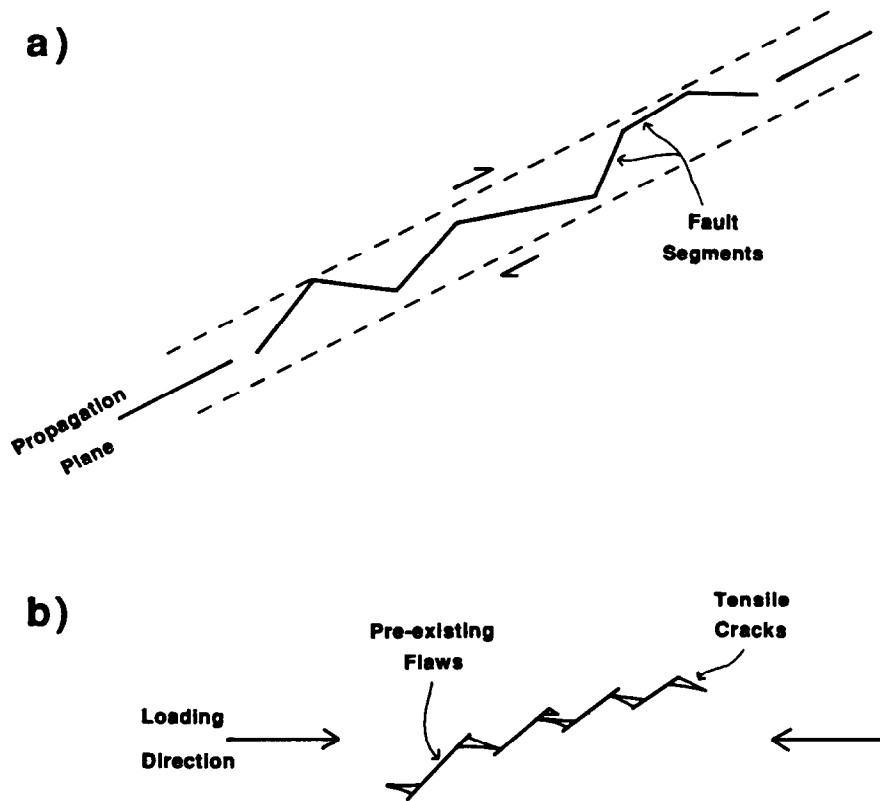
Fig. 15. (a) Zig-zag or sawtooth fault geometry of the laboratory shear fracture. The dashed lines indicate a hypothetical limit to the distance that a given oblique segment may extend from the overall fault plane. (b) Sketch of the model for shear-fracture formation proposed by Horii & Nemat-Nasser (1985) and Ashby & Hallam (1986). During axial loading under confining pressure, planes of pre-existing, inclined flaws, commonly cracks or biotite crystals (Gottschalk *et al.* 1990), become connected by tensile cracks extending out from their edges, which eventually leads to failure along the interconnected network. The tensile and pre-existing cracks of the model fault have a superficial correspondence to the segments of the laboratory fault in (a), but details of their origin differ.
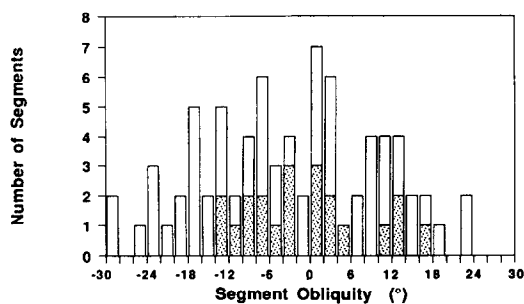

Fig. 16. Deviation of fault segments from the average strike; (+) angles denote segments that trend towards the compressional side of the fault, and (−) angles are for segments that trend towards the dilational side. The 70 mm extent of the fault visible in thin sections A and B was measured; segments from the 25 mm stretch farthest from the fracture tip are indicated by the shading. A few segments fall outside the ±30° range included in the figure; nearly all of them are in the 45 mm extent closer to the fracture tip.

form throughout the sample, and they have a roughly axial orientation. Following initiation of the shear fracture, microcracking becomes concentrated in a process zone that extends at least 8–10 mm in front of the fracture tip, and these microcracks are oriented, on average, at 30° to the fault strike. A possibly later stage of process-zone cracking, oriented at smaller angles to

the fault, is concentrated directly in front of the fracture tip. These less obliquely oriented cracks may form links between the earlier-formed tensile cracks, producing a connected network of cracks that eventually leads to extension of the rupture.

(4) The expected microcrack damage in front and to the sides of the fault, estimated from models of the stress field associated with the fault, is consistent with the measured crack densities. Preliminary calculations suggest that the energy release rate G_{II} for mode II fracture propagation is at least $1.7\text{–}8.6\ \mathrm{kJ\ m^{-2}}$. The new surface area created by microcracking in the process zone may therefore account for a significant proportion of the energy dissipated during shear-fracture propagation.

(5) The microcrack fabric and density variations in the process zone facilitate the development of fault segments that trend away from the average fault strike towards the dilational quadrant. After following such a path for some distance, the propagating shear must eventually reverse directions, in order to maintain an overall in-plane propagation path. The result is a zig-zag pattern of fault segments, which becomes more subdued but does not disappear completely with increasing displacement and the accompanying generation of a wide crushed zone. The sawtooth geometry is thus an inevi-

table consequence of mode II fault propagation by means of a process zone, and it may be characteristic of faults of various types in nature.

REFERENCES

Ashby, M. F. & Hallam, S. D. 1986. The failure of brittle solids containing small cracks under compressive states. *Acta metall.* **34**, 497–510.

Ashby, M. F. & Sammis, C. G. 1990. The damage mechanics of brittle solids in compression. *Pure Appl. Geophys.* **133**, 489–521.

Atkinson, B. K. (editor) 1987. *Fracture Mechanics of Rock.* Academic Press, New York.

Bilham, R. & King, G. 1989. Slip distribution and oblique segments of the San Andreas fault, California: observations and theory. In: *Fault Segmentation and Controls of Rupture Initiation and Termination* (edited by Schwartz, D. P. & Sibson, R. H.). U.S. Geol. Surv. Open-File Rep. 89-315, 80-93.

Bilham, R. & Williams, P. 1985. Sawtooth segmentation and deformation processes on the southern San Andreas fault, California. *Geophys. Res. Lett.* **12**, 557–560.

Chayes, F. 1950a. Composition of the granites of Westerly and Bradford, Rhode Island. *Am. J. Sci.* **248**, 378–407.

Chayes, F. 1950b. On a distinction between late-magmatic and post-magmatic replacement reactions. *Am. J. Sci.* **248**, 22–36.

Cox, S. J. D. & Scholz, C. H. 1988. On the formation and growth of faults: an experimental study. *J. Struct. Geol.* **10**, 413–430.

Dale, T. N. 1923. The Commercial Granites of New England. *Bull. U.S. geol. Surv.* **738**.

Douglass, P. M. & Voight, B. 1969. Anisotropy of granites: a reflection of microscopic fabric. *Géotechnique* **19**, 376–398.

Engelder, T. 1987. Joints and shear fractures in rock. In: *Fracture Mechanics of Rock* (edited by Atkinson, B. K.). Academic Press, London, 27–69.

Fischer, M. P. 1992. Strain energy density factor: A potential fracture mechanics fault propagation criterion. *Geol. Soc. Am. Abs. Progr.* **24**, 245–246.

Fredrich, J. T. & Wong, T.-F. 1986. Micromechanics of thermally induced cracking in three crustal rocks. *J. geophys. Res.* **91**, 12743–12764.

Gottschalk, R. R., Kronenberg, A. K., Russel, J. E. & Handin, J. 1990. Mechanical anisotropy of gneiss: Failure criterion and textural sources of directional behavior. *J. geophys. Res.* **95**, 21613–21634.

Granier, T. 1985. Origin, damping, and pattern of development of faults in granites. *Tectonics* **4**, 721–737.

Hadley, K. 1976. Comparison of calculated and observed crack densities and seismic velocities in Westerly granite. *J. geophys. Res.* **81**, 3484–3494.

Horii, H. & Nemat-Nasser, S. 1985. Compression-induced microcrack growth in brittle solids: axial splitting and shear fracture. *J. geophys. Res.* **90**, 3105–3125.

Howarth, D. F. 1987. The effect of pre-existing microcavities on mechanical rock performance in sedimentary and crystalline rocks. *Int. J. Rock Mech. Min. Sci. Geomech. Abs.* **24**, 223–233.

King, G. & Yielding, G. 1984. The evolution of a thrust fault system: processes of rupture initiation, propagation and termination in the 1980 El Asnam (Algeria) earthquake. *Geophys. J. R. astr. Soc.* **77**, 915–933.

Kranz, R. L. 1979. Crack growth and development during creep of Barre granite. *Int. J. Rock Mech. Min. Sci. Geomech. Abs.* **16**, 23–35.

Kranz, R. L. 1983. Microcracks in rocks: a review. *Tectonophysics* **100**, 449–480.

Kronenberg, A. K., Kirby, S. H. & Pinkston, J. 1990. Basal slip and mechanical anisotropy of biotite. *J. geophys. Res.* **95**, 19257–19278.

Lockner, D. A. 1993. Room temperature creep in saturated granite. *J. geophys. Res.* **98**, 475–487.

Lockner, D. A., Byerlee, J. D., Kuksenko, V., Ponomarev, A. & Sidorin, A. 1991. Quasi-static fault growth and shear fracture energy in granite. *Nature* **350**, 39–42.

Lockner, D. A., Byerlee, J. D., Kuksenko, V., Ponomarev, A. & Sidorin, A. 1992a. Observations of quasi-static fault growth from acoustic emissions. In: *Fault Mechanics and Transport Properties of Rocks* (edited by Evans, B. & Wong, T.-F.). Academic Press, San Diego, 3–31.

Lockner, D. A. & Madden, T. R. 1991. A multiple-crack model of brittle fracture 1. Non-time-dependent simulations. *J. geophys. Res.* **96**, 19,623–19,643.

Lockner, D. A., Moore, D. E. & Reches, Z. 1992b. Microcrack interaction leading to shear fracture. *Proc. Thirty-third U.S. Symp. Rock Mech.* 807–816.

Madden, T. H. 1983. Microcrack connectivity in rocks: a renormalization group approach to the critical phenomena of conduction and failure in crystalline rocks. *J. geophys. Res.* **88**, 585–592.

Moore, D. E. 1993. Microcrack Populations Associated with a Propagating Shear Fracture in Granite. U.S. Geol. Surv. Open-File Rep. 93-245.

Moore, D. E., Morrow, C. A. & Byerlee, J. 1987. Fluid-rock interaction and fracture development in 'crystalline' rock types. U.S. Geol. Surv. Open-file Rep. 87-279.

Moore, D. E., Summers, R. & Byerlee, J. D. 1990. Faults, fractures, and other deformation features produced during loading of granite in triaxial equipment. U.S. Geol. Surv. Open-File Rep. 90-349.

Paterson, M. S. 1958. Experimental deformation and faulting in Wombeyan marble. *Bull. geol. Soc. Am.* **69**, 465–476.

Peng, S. & Johnson, A. M. 1972. Crack growth and faulting in cylindrical specimens of Chelmsford granite. *Int. J. rock Mech. Min. Sci. Geomech. Abs.* **9**, 37–86.

Pollard, D. D. & Segall, P. 1987. Theoretical displacements and stresses near fractures in rock: with application to faults, joints, veins, dikes, and solution surfaces. In: *Fracture Mechanics of Rock* (edited by Atkinson, B. K.). Academic Press, London, 277–349.

Rice, J. R. (editor) 1980. *The Mechanics of Earthquake Rupture.* North Holland, Amsterdam.

Segall, P. & Pollard, D. D. 1983. Nucleation and growth of strike-slip faults in granite. *J. geophys. Res.* **88**, 555–568.

Simmons, G., Todd, T. & Baldridge, W. S. 1975. Toward a quantitative relationship between elastic properties and cracks in low porosity rocks. *Am. J. Sci.* **275**, 318–345.

Sprunt, E. S. & Brace, W. F. 1974. Direct observation of microcracks in crystalline rocks. *Int. J. Rock Mech. Min. Sci. Geomech. Abs.* **11**, 139–150.

Sprunt, E. S. & Nur, A. 1979. Microcracking and healing in granites: new evidence from cathodoluminescence. *Science* **205**, 495–497.

Tapponnier, P. & Brace, W. F. 1976. Development of stress-induced microcracks in Westerly granite. *Int. J. Rock Mech. Min. Sci. Geomech. Abs.* **13**, 103–112.

Tullis, J. & Yund, R. A. 1977. Experimental deformation of dry Westerly granite. *J. geophys. Res.* **82**, 5705–5718.

Wong, T.-F. 1982a. Micromechanics of faulting in Westerly granite. *Int. J. Rock. Mech. Min. Sci. Geomech. Abs.* **19**, 49–64.

Wong, T.-F. 1982b. Shear fracture energy of Westerly granite from post-failure behavior. *J. geophys. Res.* **87**, 990–1000.

Wong, T.-F. 1985. Geometric probability approach to the characterization and analysis of microcracking in rocks. *Mech. Mat.* **4**, 261–276.